


 Cite this: *Nanoscale*, 2023, 15, 1669

Integrated structure design and synthesis of a pitaya-like SnO₂/N-doped carbon composite for high-rate lithium storage capability†

 Xiao Liu,^{a,b} Shuai Zhang,^a Peng Zhang,^{id}*^c Zongmin Zheng,^{id}^d Feng Bai^a and Qi Li^{id}*^a

Tin dioxide (SnO₂) with a high theoretical capacity of 1494 mA h g⁻¹ has great potential to break through the capacity limitation of the conventional graphite anode (372 mA h g⁻¹) in lithium-ion batteries. However, its practical application still faces several obstacles such as high volumetric expansion and poor electrical conductivity. To solve these problems, innovative design and synthesis of SnO₂-based nanocomposite structures are necessary. Herein, we demonstrate an integrated design of a hierarchical pitaya-like P-SnO₂/C@NC core-shell nanostructure which includes the core of SnO₂ nanoparticles (~4–12 nm) uniformly embedded in the porous carbon sphere and the shell of a continuous nitrogen-doped carbon (NC) layer. Specifically, during repetitive lithiation and delithiation processes, the ultrasmall SnO₂ nanoparticles reduce the internal stress greatly, the porous carbon matrix provides buffer space for a large volume change, and the N-doped carbon shell further guarantees the whole structure unit sufficient electrical conductivity and structural stability. Consequently, the resultant battery exhibits a reversible capacity of 936.8 mA h g⁻¹ after 100 cycles at 100 mA g⁻¹ and even an average capacity of 460.0 mA h g⁻¹ at a high current density of 3.2 A g⁻¹. The excellent electrochemical performance of pitaya-like SnO₂/C@NC proves the efficacy of this structure design and thus provides significant reference for the construction of other electrode materials in rechargeable alkali metal ion batteries.

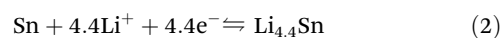
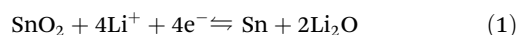
 Received 14th October 2022,
Accepted 29th November 2022
DOI: 10.1039/d2nr05702f

rsc.li/nanoscale

Introduction

With the booming development of portable electrical devices and electric vehicles, energy storage devices with high rate and high capacity are urgently needed.^{1–5} Among them, lithium-ion batteries (LIBs) have received much attention due to their high energy density and long cycle life.^{6–10} To break through the current capacity limitation of LIBs, exploring promising alternative anode materials beyond the traditional graphite

has been regarded as one of the most feasible strategies.^{11–13} Various materials such as Co₃O₄, Fe₂O₃, Mn₃O₄ and SnO₂ with a high theoretical capacity have attracted much attention,^{14–20} especially SnO₂ due to its higher theoretical capacity, low toxicity and natural abundance.^{21–25} The specific electrochemical pathways of SnO₂ with lithium include both conversion (eqn (1)) and alloying reactions (eqn (2)). The reversibility of the conversion reaction is mainly limited by the size of the particles, highlighting the importance of the size effect.^{26,27} Next step, the alloying process between Sn and Li contributes to the major capacity,^{28,29} but this process is accompanied by pulverization and aggregation due to large volume expansion (300% upon full lithiation), resulting in fast capacity fading and poor rate performance.³⁰ Over the past few decades, though tremendous efforts have been devoted to optimize the SnO₂ anode for next generation LIBs, the above two critical issues still perplex us to some extent.^{31,32}



According to the reaction pathways, nanostructural design of SnO₂, such as nanowires, nanotubes and hollow nano-

^aKey Lab for Special Functional Materials of Ministry of Education, National & Local Joint Engineering Research Center for High-efficiency Display and Lighting Technology, Collaborative Innovation Center of Nano Functional Materials and Applications, School of Materials Science and Engineering, Henan University, Kaifeng 475004, P. R. China. E-mail: nanokingdom@163.com

^bCollege of Chemistry and Chemical Engineering, Henan Key Laboratory of Function-Oriented Porous Materials, Luoyang Normal University, Luoyang, 471934, P. R. China

^cDepartment of Chemistry, College of Sciences, Northeastern University, Shenyang, 110819 Liaoning, P. R. China

^dNational Engineering Research Center for Intelligent Electrical Vehicle Power System, College of Mechanical and Electrical Engineering, Qingdao University, Qingdao, Shandong, 266071, P. R. China

† Electronic supplementary information (ESI) available. See DOI: <https://doi.org/10.1039/d2nr05702f>

spheres, is believed to be a promising method to provide better reversibility because of its controllable internal strain caused by lithiation/delithiation.^{32–35} Meanwhile, nanostructured SnO₂ can effectively shorten the Li-ion diffusion pathway and consequently improve the rate capability to some extent.^{36,37} However, the intrinsic low electronic conductivity of SnO₂ still constrains its rate capability; likewise pulverization caused by the large volume expansion limits the cycling stability.³⁸ To solve these two problems, loading SnO₂ nanostructures on various types of conductive carbon substrates is put forward to improve the conductivity and structural stability of SnO₂.^{39–43} Simultaneously, the porous design of the carbon substrate is developed to further accommodate the large volume change and promote the rapid transmission of Li⁺.⁴⁴ Nevertheless, SnO₂ nanoparticles that directly grow on the surface layer of the carbon materials would still migrate and aggregate during long cycles.^{31,32} Therefore, for driving SnO₂ to substantially overcome its defects and further increase the stability, realization of an advanced and integrated structural innovation is urgently needed.

In this work, we have designed and synthesized a core-shell structured SnO₂-based composite where ultrasmall SnO₂ nanoparticles are uniformly embedded in porous carbon nanospheres and there is a continuous N-doped carbon coating layer on the surface (denoted as P-SnO₂/C@NC). The pitaya-like composites not only improve the electrical conductivity of SnO₂, but also alleviate its expansion and aggregation during the lithiation/delithiation process. More importantly, the N-doped carbon shell can act as an armor to ensure the structure stability of the SnO₂/carbon composite during cycling. As expected, the obtained P-SnO₂/C@NC gives a high reversible capacity of 936.8 mA h g⁻¹ at 100 mA g⁻¹ after 100 cycles and superior rate performance. The excellent performance can be attributed to the unique pitaya-like structure of P-SnO₂/C@NC and thus provides significant reference for the synthesis of other electrode materials for rechargeable alkali metal ion batteries.

Experimental

Materials

Ethylene glycol dimethacrylate was purchased from TCI, Shanghai, China. Azobisisobutyronitrile (AIBN) was obtained from Shisihewei, Shanghai, China. Acetonitrile, α -methacrylic acid and sodium acetate anhydrous were received from Aladdin, Shanghai, China. Dehydrated alcohol was purchased from Anhui Ante, China. Tin(II) chloride dihydrate was obtained from J&K, China. Graphene nanosheets (GSS) were prepared by Hummers' method.

Preparation of the polymer microsphere precursor (pMS)

As described in our published report,⁴⁵ ethylene glycol dimethacrylate (2.0 g, 10.1 mmol), α -methacrylic acid (8.0 g, 93.1 mmol), and AIBN (0.2067 g, 2 wt% relative to the comonomers) were dissolved in 400 mL of acetonitrile in a dried two-

necked flask. A typical procedure of distillation precipitation copolymerization was carried out. After the polymerization, the resultants were purified with dehydrated alcohol. Then, pMS with a diameter of about 350 nm was obtained.

Preparation of Sn-pMS

Sn-pMS was synthesized by a facile cation exchange method. Firstly, sodium acetate anhydrous (0.984 g) was dissolved in dehydrated alcohol (100 mL), and then pMS (300 mg) was added under continuous stirring for 12 h. After centrifugation, the precipitate was washed with dehydrated alcohol several times and then poured into 100 mL dehydrated alcohol with tin(II) chloride dihydrate (0.6768 g). The resultant product was collected by centrifugation after 24 h. Finally, Sn-pMS was obtained after freeze-drying.

Preparation of monodisperse pre-oxidized nanospheres

Sn-pMS powders were oxidized in air at 300 °C for 4 h at the rate of 1 °C min⁻¹. Subsequently, the pre-oxidized nanospheres (0.2 g) were dispersed in water (70 mL) by sonication. Then, the resulting products were transferred into 100 mL Teflon-lined stainless-steel autoclaves and maintained at 150 °C for 5 h. Finally, monodisperse pre-oxidized nanospheres were obtained.

Preparation of pitaya-like P-SnO₂/C@NC, SnO₂/C and yolk-shell SnO₂ nanospheres

Firstly, monodisperse pre-oxidized nanospheres (0.2 g) were dispersed in Tris-buffer solution (10 mM). Then, 200 mg dopamine was added and it would polymerize on the surface of the nanospheres. Next, SnO₂/C@PDA nanospheres were obtained by centrifugation and freeze-drying. Finally, the pitaya-like P-SnO₂/C@NC nanospheres were obtained after calcination under a N₂ atmosphere at 500 °C for 3 h, SnO₂/C nanospheres were obtained by annealing P-SnO₂/C@NC at 400 °C for 1 h under air, and yolk-shell SnO₂ nanospheres were obtained by annealing P-SnO₂/C@NC nanospheres at 500 °C for 2 h under air.

Preparation of SnO₂/GSS

Firstly, GSS (10 mg), SnCl₂·2H₂O (20 mg), and concentrated HCl (0.5 mL) were dispersed in deionized water (25 mL) to form a solution. Subsequently, the solution was stirred at 40 °C for 4 h. Then, the resultant products were collected by centrifugation and washed with deionized water. Finally, the SnO₂/GS composite was obtained after calcination at 400 °C in air for 2 h.

Results and discussion

P-SnO₂/C@NC nanospheres were synthesized by a simple cation exchange and subsequent calcination method (Fig. 1a). The process is described as follows: firstly, carboxyl-rich polymer microsphere (pMS, Fig. S1a[†]) precursors were prepared by copolymerization of ethylene glycol dimethacrylate

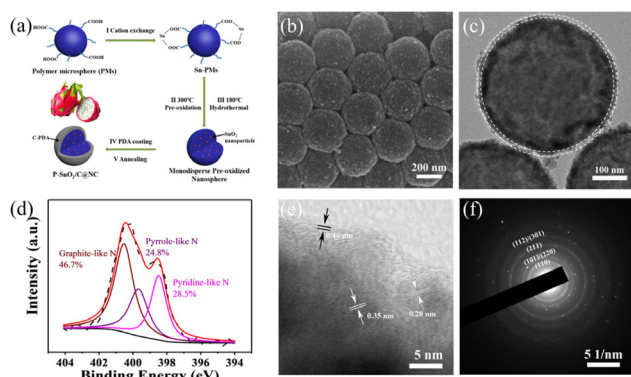


Fig. 1 (a) Schematic illustration of the fabrication of pitaya-like P-SnO₂/C@NC. (b) SEM image, (c) TEM image of P-SnO₂/C@NC. (d) N 1s XPS spectrum of P-SnO₂/C@NC. (e) HRTEM image and (f) SAED pattern of P-SnO₂/C@NC.

and α -methacrylic acid. Subsequently, Sn-pMS was obtained after Na⁺ and Sn²⁺ cation exchange (Fig. S1b[†]). To investigate this process in depth, Fourier Transform Infrared spectroscopy (FTIR) that can characterize the elaborate structure of chemical bonds was carried out. In the FTIR spectrum, the pMS had a strong and broad peak at 3206 cm⁻¹ due to the vibration of the -OH stretching of the carboxylic acid group (Fig. S2a[†]). At the same time, there were two strong peaks at 1713 and 1166 cm⁻¹ corresponding to the stretching vibration of the R2C=O group of the carboxylic acid and the -C-O-C- group of ethylene glycol dimethacrylate, respectively (Fig. S2b[†]). After adding sodium acetate anhydrous, the vibration of -OH stretching at 3206 cm⁻¹ disappeared and the intensity decreased significantly. Meanwhile, the new peak at 1556 cm⁻¹ can be attributed to the asymmetric stretching vibration of carboxylates. This result demonstrates that the coordination of the carboxylic acid group with the sodium ion may take place. After exchange with tin ions, it can be seen that the asymmetric stretching vibration of carboxylates shifts to a low wavenumber of 1544 cm⁻¹. In addition, energy-dispersive X-ray spectroscopy (EDS) elemental analysis also demonstrates this process (Fig. S3[†]). Then, monodisperse nanospheres (Fig. S4a[†]) were obtained by pre-oxidation and hydrothermal treatment of Sn-pMS. Finally, P-SnO₂/C@NC nanospheres were obtained by PDA (polymerized dopamine) coating (Fig. S4b[†]) and the subsequent calcination. XRD patterns (Fig. S5,† purple line) confirm the existence of rutile SnO₂ (JCPDS 41-1445) in P-SnO₂/C@NC without any other impurities. As shown in scanning electron microscopy (SEM) images (Fig. 1b), the final product P-SnO₂/C@NC exhibits a similar morphology to pMS after calcination, and the diameter of P-SnO₂/C@NC is about 350 nm. The inner structure of P-SnO₂/C@NC was further investigated by transmission electron microscopy (TEM) (Fig. 1c), from which it can be seen that SnO₂ nanoparticles are uniformly distributed in the carbon matrix and the intact calcined PDA thin layer around 5–10 nm is also clearly distinguished on the surface of the structure unit. It is believed that the obtained carbon matrix in the core and the calcined PDA

shell layer can effectively prevent the migration and aggregation of SnO₂ nanoparticles during the electrochemical reaction besides the improved electrical conductivity. From a representative high-resolution TEM (HRTEM) image (Fig. 1e and Fig. S6[†]), the particle size of SnO₂ was found to be approximately 4–12 nm, and the characteristic lattice fringe spacing of 0.35 and 0.28 nm can be assigned to the (110) and (101) planes of rutile SnO₂, respectively. In addition, the calcined PDA also shows a stacked layer with the lattice fringe spacing of about 0.40 nm. Diffraction rings in the selected-area electron diffraction (SAED) pattern further prove the rutile structure of SnO₂ (Fig. 1f), which is consistent with the XRD results in Fig. S5.† Furthermore, the X-ray photoelectron spectroscopy (XPS) results confirm the existence of C, N, O and Sn elements in P-SnO₂/C@NC, and the high-resolution N 1s spectrum contains three types of nitrogen species, including pyridinic N (398.5 eV, 28.5%), pyrrolic N (399.7 eV, 24.8%) and graphitic N (400.5 eV, 46.7%) (Fig. 1d). From the above results, we can see that the as-prepared P-SnO₂/C@NC nanospheres simultaneously combine several appealing features including ultra-small SnO₂, a highly conductive and porous carbon matrix, and a uniform N-doped carbon coating layer.

To gain insight into the novel structure of P-SnO₂/C@NC, two typical SnO₂-based materials including SnO₂ nanoparticles embedded in carbon nanospheres (denoted as SnO₂/C) and yolk-shell SnO₂ nanospheres were obtained from P-SnO₂/C@NC for comparison (Fig. 2a). After insufficient calcination in air to remove the N-doped carbon layer, SnO₂/C nanospheres were obtained. According to the TEM image, SnO₂/C exhibited a similar morphology to P-SnO₂/C@NC, but the surface was coarse and SnO₂ nanoparticles were exposed on

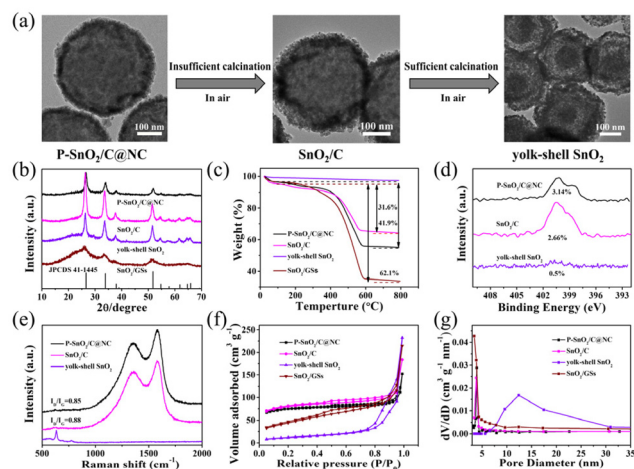


Fig. 2 (a) Schematic illustration of conversion of P-SnO₂/C@NC to SnO₂/C and yolk-shell SnO₂ and the corresponding TEM images. (b) XRD patterns, (c) TGA curves of P-SnO₂/C@NC (black line), SnO₂/C (magenta line), yolk-shell SnO₂ (violet line) and SnO₂/GSs (wine line), (d) N 1s XPS spectra, (e) Raman spectra of P-SnO₂/C@NC, SnO₂/C and yolk-shell SnO₂. (f) N₂ adsorption-desorption isotherms and (g) pore size distribution of P-SnO₂/C@NC, SnO₂/C, yolk-shell SnO₂ and SnO₂/GSs.

the surface. When the carbon matrix is completely removed, yolk-shell SnO₂ nanospheres are obtained. Similar yolk-shell metallic oxide nanospheres have been synthesized using a developed sequential template method by Wang's and Lou's groups^{46,47} In addition, in order to confirm the role of the barrier matrix, SnO₂ nanoparticles loaded on graphene nanosheets (denoted as SnO₂/GSs) were also synthesized by a previously reported method.⁴⁸ From the SEM and TEM images (Fig. S7a and S7b[†]), it can be seen that a large amount of ultra-small SnO₂ nanoparticles anchored on GSs. All the diffraction peaks of SnO₂/C, yolk-shell SnO₂ and SnO₂/GSs can be indexed to rutile SnO₂ (Fig. 2b). It is worth noting that the diffraction peaks of SnO₂/GSs are relatively broad, indicating the smaller crystal size of SnO₂ nanoparticles, which is consistent with the SEM and TEM results. The weight ratios of SnO₂ in P-SnO₂/C@NC, SnO₂/C, yolk-shell SnO₂ and SnO₂/GSs determined by thermogravimetric analysis (TGA) are 58.1%, 68.4%, 97.5% and 37.9%, respectively (Fig. 2c). The decrease of N content (Fig. 2d) and increase of Sn content (Fig. S8[†]) also proved that the N-doped carbon coating layer and carbon matrix were gradually removed. In the Raman spectra, the D band and G band corresponding to disordered and graphitic carbon centered at 1355 and 1575 cm⁻¹, respectively (Fig. 2e). The I_D/I_G ratio can be used to estimate the average size of the graphitic domains, and the value for P-SnO₂/C@NC and SnO₂/C is about 0.85 and 0.88, respectively, indicating a high graphitization degree after calcination. Nitrogen adsorption-desorption isotherms of P-SnO₂/C@NC, SnO₂/C, yolk-shell SnO₂ and SnO₂/GSs show a typical type-IV curve with a hysteresis loop (Fig. 2f). The corresponding pore size distributions of these samples based on the Barrett-Joyner-Halenda (BJH) model demonstrate the existence of abundant mesoporous (Fig. 2g). Such a porous structure gives rise to a high Brunauer-Emmett-Teller (BET) specific surface area of P-SnO₂/C@NC, SnO₂/C, yolk-shell SnO₂ and SnO₂/GSs of 248, 230, 44 and 165 m² g⁻¹, respectively. The numerous mesopores in all the samples provide the function of accommodating the large volume change and also accelerating the lithium insertion/extraction during charge and discharge processes. Through the design and comparison of these pertinent samples, we could further learn the critical role of the NC coating layer as well as the importance of structure optimization.

Intrigued by the advanced structural features of P-SnO₂/C@NC, we have evaluated the electrochemical performance of the above samples. EIS results show that the charge transfer resistance of P-SnO₂/C@NC is slightly higher than that of SnO₂/GSs, but obviously lower than that of SnO₂/C and yolk-shell SnO₂ (Fig. 3a), indicating the superior conductivity of P-SnO₂/C@NC. The decreased conductivity of SnO₂/C and yolk-shell SnO₂ can be attributed to the removal of the conductive N-doped carbon layer and the carbon matrix during the post-calcination process (Fig. 2a). Fig. 3b shows the CV curves of P-SnO₂/C@NC in the initial three cycles, and a pronounced reduction peak at 0.72 V in the first cycle can be assigned to the reduction of SnO₂ to Sn and the formation of a solid-electrolyte-interphase layer (SEI), and another reduction peak at

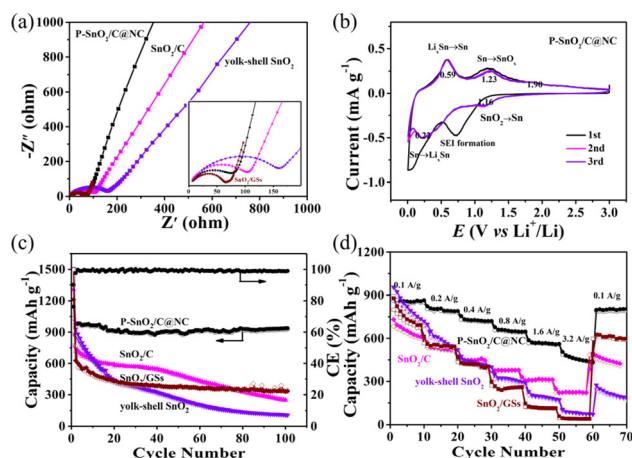


Fig. 3 Electrochemical performance of P-SnO₂/C@NC, SnO₂/C, yolk-shell SnO₂ and SnO₂/GS electrodes. (a) EIS spectra of P-SnO₂/C@NC, SnO₂/C, yolk-shell SnO₂ and SnO₂/GS electrodes. (b) CV curves of P-SnO₂/C@NC electrodes in the initial three cycles between 5 mV and 3.0 V at a scan rate of 0.1 mV s⁻¹. (c) Cycling performance and (d) rate capability of P-SnO₂/C@NC, SnO₂/C, yolk-shell SnO₂ and SnO₂/GS electrodes.

0.05 V can be attributed to the alloying process of Li and Sn.⁴⁴ During the anodic scan, a strong peak at 0.59 V and a broad peak at 1.23 V correspond to the delithiation of Li_xSn to Sn and the oxidation of metallic Sn, respectively.³⁰ In the subsequent cycles, the CV curves almost overlap, suggesting the excellent electrochemical reversibility of the P-SnO₂/C@NC electrode. However for SnO₂/C, yolk-shell SnO₂ and SnO₂/GSs, the peak current decreases continuously with the CV cycling (Fig. S9a-c[†]). In addition, when comparing the third cycle of P-SnO₂/C@NC, SnO₂/C, yolk-shell SnO₂ and SnO₂/GSs (Fig. S9d[†]), P-SnO₂/C@NC shows the smallest peak separation (70 mV) for the reversible peaks located near 1.20 V, demonstrating the less overpotential for the phase transformation between Sn and SnO₂ for the P-SnO₂/C@NC electrode than the others. Galvanostatic charge/discharge tests were further performed to evaluate the electrochemical performance of the above samples in the potential window of 3.0–0.005 V at a constant current density of 0.1 A g⁻¹ (Fig. 3c and S10[†]). After 100 cycles, P-SnO₂/C@NC still delivers a discharge capacity of about 936.8 mA h g⁻¹ with a high coulombic efficiency close to 99.0%. The excellent capacity retention should benefit from improved electron transfer with an N-doped carbon coating layer and the ultrasmall SnO₂ nanoparticle embedded in a porous carbon matrix. In contrast, the capacity of SnO₂/C, yolk-shell SnO₂ and SnO₂/GSs significantly decreased down to 250.5, 107.7 and 342.3 mA h g⁻¹, respectively. The first coulombic efficiency (CE) for P-SnO₂/C@NC, SnO₂/C, yolk-shell SnO₂ and SnO₂/GSs was 76.3%, 59.2%, 58.6% and 57.9%, respectively. The loss of capacity is mainly caused by the irreversible formation of SEI films. From the second cycle, the CE of P-SnO₂/C@NC increases quickly to nearly 100%, and poor conductivity and no carbon matrix are responsible for the low capacity retention for SnO₂/C and yolk-shell SnO₂. Though

SnO₂/GSs has good conductivity, the exposure of SnO₂ nanoparticles on the surface of GSs inevitably leads to the aggregation during cycling, thus giving low capacity retention. Fig. 3d compares the rate performance of P-SnO₂/C@NC, SnO₂/C, yolk-shell SnO₂ and SnO₂/GSs at current densities of 0.1, 0.2, 0.4, 0.8, 1.6 and 3.2 A g⁻¹. The P-SnO₂/C@NC electrode also exhibits optimal performance at high current densities, and the average value is 851.0, 791.0, 720.2, 647.9, 562.3 and 455.5 mA h g⁻¹, respectively. More importantly, the discharge capacity can be recovered to 805.2 mA h g⁻¹ when the current density returns to 0.1 A g⁻¹. In contrast, SnO₂/C, yolk-shell SnO₂ and SnO₂/GSs give a much lower capacity of 225.8, 83.4 and 40 mA h g⁻¹ at 3.2 A g⁻¹, respectively. In addition, the cycling performance of the P-SnO₂/C@NC electrode at a high current density of 0.4 A g⁻¹ can maintain 690 mA h g⁻¹ even after 100 cycles (Fig. S11†). These results demonstrate the excellent energy density and high-rate capability of the P-SnO₂/C@NC composite.

In order to have an in-depth understanding of the lithium storage behavior in P-SnO₂/C@NC, SnO₂/C and yolk-shell SnO₂ electrodes, a series of CV tests with scan rates between 0.1 and 10 mV s⁻¹ were carried out (Fig. 4). According to a power law relationship $i = av^b$ ($\log i = \log a + b \log v$, where i is the peak current, v is the scan rate, a and b are adjustable parameters), b values obtained from the slope of the plot of $\log i$ vs. $\log v$ can be used to describe the reaction kinetics (Fig. 4d). There are two well-defined conditions: $b = 0.5$ and $b = 1.0$. For $b = 0.5$, the limiting case would be a diffusion-controlled process, while $b = 1.0$ is representative of a surface controlled process, which also means that the reaction rate is rapid.²⁸ At a low scan rate of 0.1–1.0 mV s⁻¹, all b values are calculated in the range of 0.8–1.0 for P-SnO₂/C@NC (Table S1†), indicating a major surface controlled process, while for SnO₂/C and yolk-shell SnO₂ (Fig. S12 and Table S1†),

b values for the conversion reaction drop to 0.7, implying a combination of solid state diffusion and surface limited reactions. At higher scan rates between 1.0 and 10 mV s⁻¹, for P-SnO₂/C@NC, all b values are still greater than 0.5, while for SnO₂/C and yolk-shell SnO₂, some b values are below 0.5, which means that SnO₂/C and yolk-shell SnO₂ are mainly controlled by the diffusion process at a higher scan rate.

To understand the difference in the electrochemical performance, the morphology and structure changes of the corresponding electrodes after charge–discharge cycles were investigated. SEM images reveal that P-SnO₂/C@NC (Fig. 5a) and SnO₂/C (Fig. 5c) still maintain the spherical shape after 100 cycles, while the framework of yolk-shell SnO₂ collapsed, which accounts for its low electrochemical performance (Fig. S13a†). TEM images were obtained to further investigate the inner structure. It can be seen that the SnO₂ nanoparticles become smaller in P-SnO₂/C@NC (Fig. 5b), while the SnO₂ nanoparticles agglomerate into larger ones in SnO₂/C (Fig. 5d), and no complete microsphere is observed in yolk-shell SnO₂ (Fig. S13b†). These results unambiguously demonstrate the key role of the N-doped carbon coating layer in preventing the agglomeration of SnO₂ nanoparticles and maintaining the stability of the structure unit. The disappearance of the characteristic XRD peaks of rutile SnO₂ in both P-SnO₂/C@NC and SnO₂/C suggests the amorphous nature of SnO₂ after cycling (Fig. 5e). The XPS results demonstrate that Sn 3d peaks slight shift to higher energies after charging (Fig. 5f), and the variation could be attributed to a more negative ion combining with Sn⁴⁺.⁴⁹ The possible reaction mechanism can be conjectured as follows: due to the poor electrical conductivity of SnO₂/C and yolk-shell SnO₂, the reduction of SnO₂ nanoparticles starts at the contact point between the current collector and the SnO₂ nanoparticles; particles away from the current collector must wait for the reaction front to arrive from adjacent particles, thus the particle size will grow gradually. While for P-SnO₂/C@NC, the reduction front radiates inward from the entire surface due to the enhancement of surface conductivity by the N-doped carbon coating layer. After the

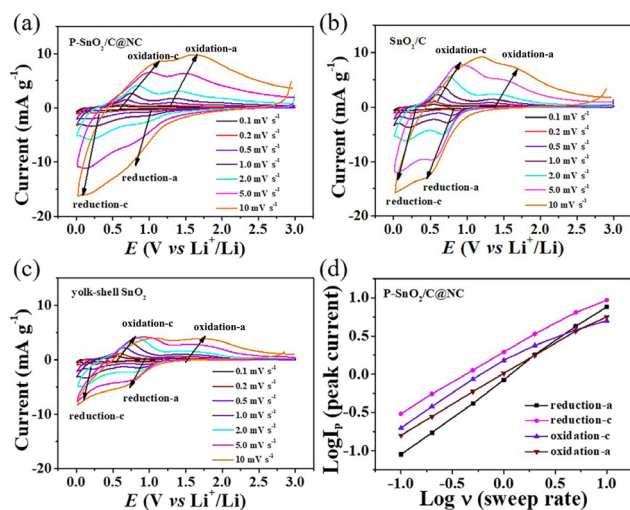


Fig. 4 Kinetics analysis of P-SnO₂/C@NC, SnO₂/C and yolk-shell SnO₂. CVs at different scan rates of (a) P-SnO₂/C@NC, (b) SnO₂/C, and (c) yolk-shell SnO₂. (d) Plots of $\log i_p$ versus $\log v$ curves of cathodic and anodic peaks in P-SnO₂/C@NC.

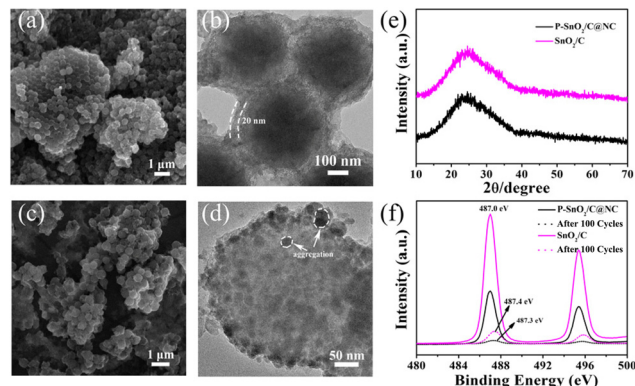


Fig. 5 (a, c) SEM and (b, d) TEM images of P-SnO₂/C@NC (a, b) and SnO₂/C (c, d) electrodes after cycling. (e) XRD pattern and (f) XPS spectra of P-SnO₂/C@NC and SnO₂/C after cycling.

completion of the reduction reaction, each nanosphere transformed to Li_2O and fine Li_xSn precipitates decorated the carbon matrix. These fine precipitates are too small to crack, and thus they can be reversibly oxidized to SnO_2 and finally result in a stable capacity reversibility in this system.

Conclusions

In summary, we have developed an integrated structural design to effectively solve the critical issues of a SnO_2 based LIB anode. In detail, a pitaya-like $\text{P-SnO}_2/\text{C}@\text{NC}$ core-shell structure has been designed and synthesized, in which SnO_2 ultrasmall nanoparticles were uniformly embedded in the porous carbon matrix and further coated with a continuous N-doped carbon coating layer outside the matrix. The excellent electrochemical properties can be attributed to the critical role of the N-doped carbon coating layer in preventing the surface exposure of SnO_2 and maintaining the whole structure stability, the ultrathin nanostructure of SnO_2 in alleviating the pulverization and volume change expansion, and the porous carbon matrix in improving the electrical conductivity and accommodating the volume expansion. Benefiting from the unique structure optimization, the pitaya-like $\text{P-SnO}_2/\text{C}@\text{NC}$ anodes can provide a high rate capacity ($460.0 \text{ mA h g}^{-1}$ at 3.2 A g^{-1}) and excellent cycling stability (up to $936.8 \text{ mA h g}^{-1}$ after 100 cycles). This study demonstrates a paradigm of the successful structural design to solve a critical obstacle in propelling the commercial progress of SnO_2 -based anode materials for LIBs. This research also provides significant reference for the synthesis of other electrode materials in rechargeable alkali metal ion batteries.

Conflicts of interest

The authors declare no competing interests.

Acknowledgements

This work was financially supported by the Natural Science Foundation of Henan province (No. 212300410333) and the National Natural Science Foundation of China (No. 21501045).

References

- G. Xin, W. Changda, W. Wenjie, Z. Quan, X. Wenjie, Z. Pengjun, W. Shiqiang, C. Yuyang, Z. Kefu, L. Zhanfeng, Y. Xiya, W. Yixiu, W. Xiaojun, S. Li, C. Shuangming and L. Xiaosong, *Nano Res. Energy*, 2022, **1**, e9120026.
- M. Liu, W. W. Tjiu, J. Pan, C. Zhang, W. Gao and T. Liu, *Nanoscale*, 2014, **6**, 4233–4242.
- Y. Yan, S. Liang, X. Wang, M. Zhang, S.-M. Hao, X. Cui, Z. Li and Z. Lin, *Proc. Natl. Acad. Sci. U. S. A.*, 2021, **118**, e2110036118.
- Y. Yan, P. Zhang, Z. Qu, M. Tong, S. Zhao, Z. Li, M. Liu and Z. Lin, *Nano Lett.*, 2020, **20**, 7662–7669.
- M. Liu, P. Zhang, Z. Qu, Y. Yan, C. Lai, T. Liu and S. Zhang, *Nat. Commun.*, 2019, **10**, 3917.
- P. Seyedhosein, S. Florian, M. Andrey, K. Aleksandr and B. Torsten, *Nano Res. Energy*, 2022, **1**, e9120016.
- S. Zhao, Z. Wang, Y. He, B. Jiang, Y. Harn, X. Liu, F. Yu, F. Feng, Q. Shen and Z. Lin, *ACS Energy Lett.*, 2017, **2**, 111–116.
- B. Jiang, C. Han, B. Li, Y. He and Z. Lin, *ACS Nano*, 2016, **10**, 2728–2735.
- S. Zhao, Z. Wang, Y. He, H. Jiang, Y. W. Harn, X. Liu, C. Su, H. Jin, Y. Li, S. Wang, Q. Shen and Z. Lin, *Adv. Energy Mater.*, 2019, **9**, 1901093.
- D. Sui, L. Xu, H. Zhang, Z. Sun, B. Kan, Y. Ma and Y. Chen, *Carbon*, 2020, **157**, 656–662.
- Y. Li, Y. Lu, P. Adelhelm, M.-M. Titirici and Y.-S. Hu, *Chem. Soc. Rev.*, 2019, **48**, 4655–4687.
- Z. Chen, X. An, L. Dai and Y. Xu, *Nano Energy*, 2020, **73**, 104762.
- J. Mao, J. Iocozzia, J. Huang, K. Meng, Y. Lai and Z. Lin, *Energy Environ. Sci.*, 2018, **11**, 772–799.
- Y. Fu, X. Guo, Z. Xu, G. Zhao, C. Xu, Y. Zhu and L. Zhou, *ACS Appl. Mater. Interfaces*, 2021, **13**, 28171–28180.
- Z. Zheng, P. Li, J. Huang, H. Liu, Y. Zao, Z. Hu, L. Zhang, H. Chen, M.-S. Wang, D.-L. Peng and Q. Zhang, *J. Energy Chem.*, 2020, **41**, 126–134.
- Y. Jiang, J.-L. Yue, Q. Guo, Q. Xia, C. Zhou, T. Feng, J. Xu and H. Xia, *Small*, 2018, **14**, 1704296.
- S. Gao, N. Wang, S. Li, D. Li, Z. Cui, G. Yue, J. Liu, X. Zhao, L. Jiang and Y. Zhao, *Angew. Chem., Int. Ed.*, 2020, **59**, 2465–2472.
- M. Liu, H. Fan, O. Zhuo, J. Chen, Q. Wu, L. Yang, L. Peng, X. Wang, R. Che and Z. Hu, *Nano Energy*, 2020, **68**, 104368.
- Y. Chen, X. Chen and Y. Zhang, *Energy Fuels*, 2021, **35**, 6420–6442.
- Z. Wen, Z. Zhao, L. Li, Z. Sun, N. Chen, Y. Li, F. Wu and R. Chen, *Adv. Funct. Mater.*, 2022, **32**, 2109184.
- Q. Li, Y. Wang, Q. Tan, Z. Zhong and F. Su, *Chem. – Eur. J.*, 2020, **26**, 12882–12890.
- Y. S. Mun, T. N. Pham, V. K. Hoang Bui, S. T. Tanaji, H. U. Lee, G.-W. Lee, J. S. Choi, I. T. Kim and Y.-C. Lee, *J. Power Sources*, 2019, **437**, 226946.
- L. Ao, C. Wu, X. Wang, Y. Xu, K. Jiang, L. Shang, Y. Li, J. Zhang, Z. Hu and J. Chu, *ACS Appl. Mater. Interfaces*, 2020, **12**, 20824–20837.
- S. Zhao, C. D. Sewell, R. Liu, S. Jia, Z. Wang, Y. He, K. Yuan, H. Jin, S. Wang, X. Liu and Z. Lin, *Adv. Energy Mater.*, 2020, **10**, 1902657.
- L. Zhang, K. Zhao, C. Sun, R. Yu, Z. Zhuang, J. Li, W. Xu, C. Wang, W. Xu and L. Mai, *Energy Storage Mater.*, 2020, **25**, 376–381.
- B. Jiang, Y. He, B. Li, S. Zhao, S. Wang, Y.-B. He and Z. Lin, *Angew. Chem., Int. Ed.*, 2017, **56**, 1869–1872.

- 27 R. Hu, D. Chen, G. Waller, Y. Ouyang, Y. Chen, B. Zhao, B. Rainwater, C. Yang, M. Zhu and M. Liu, *Energy Environ. Sci.*, 2016, **9**, 595–603.
- 28 L. P. Wang, Y. Leconte, Z. Feng, C. Wei, Y. Zhao, Q. Ma, W. Xu, S. Bourrioux, P. Azais, M. Srinivasan and Z. J. Xu, *Adv. Mater.*, 2017, **29**, 1603286.
- 29 N. Zhang, C. Sun, Y. Huang, C. Zhu, Z. Wu, L. Lv, X. Zhou, X. Wang, X. Xiao, X. Fan and L. Chen, *J. Mater. Chem. A*, 2021, **9**, 1812–1821.
- 30 L. Zu, Q. Su, F. Zhu, B. Chen, H. Lu, C. Peng, T. He, G. Du, P. He, K. Chen, S. Yang, J. Yang and H. Peng, *Adv. Mater.*, 2017, **29**, 1701494.
- 31 S. R. Mishra and M. Ahmaruzzaman, *Nanoscale*, 2022, **14**, 1566–1605.
- 32 M. Wang, T. Chen, T. Liao, X. Zhang, B. Zhu, H. Tang and C. Dai, *RSC Adv.*, 2021, **11**, 1200–1221.
- 33 Q. Tian, Y. Chen, W. Zhang, Z. Sui and L. Yang, *J. Alloys Compd.*, 2020, **820**, 153404.
- 34 X. Zhou, L. Yu and X. W. Lou, *Nanoscale*, 2016, **8**, 8384–8389.
- 35 Q. Tian, F. Chen, Y. Liu, K. Chen and L. Yang, *Appl. Surf. Sci.*, 2019, **493**, 838–846.
- 36 F. Zoller, D. Böhm, T. Bein and D. Fattakhova-Rohlfing, *ChemSusChem*, 2019, **12**, 4140–4159.
- 37 D. S. Dalavi, R. S. Desai and P. S. Patil, *J. Mater. Chem. A*, 2022, **10**, 1179–1226.
- 38 W. Dong, J. Xu, C. Wang, Y. Lu, X. Liu, X. Wang, X. Yuan, Z. Wang, T. Lin, M. Sui, I. W. Chen and F. Huang, *Adv. Mater.*, 2017, **29**, 1700136.
- 39 K. Gong, Y. Ma, T. Zhang, L. Yan, Y. Miao and F. Gao, *Adv. Eng. Mater.*, 2021, **23**, 2100064.
- 40 B. Han, W. Zhang, D. Gao, C. Zhou, K. Xia, Q. Gao and J. Wu, *J. Power Sources*, 2020, **449**, 227564.
- 41 Y. Zhang and C. Wang, *Mater. Today Energy*, 2020, **16**, 100406.
- 42 X. Chen, H. Lu, Y. Lei, J. Zhang, F. Xiao, R. Wang, P. Xie and J. Xu, *J. Mater. Sci. Technol.*, 2022, **107**, 165–171.
- 43 P. Bhattacharya, J. H. Lee, K. K. Kar and H. S. Park, *Chem. Eng. J.*, 2019, **369**, 422–431.
- 44 X. Zhou, L. Yu and X. W. Lou, *Adv. Energy Mater.*, 2016, **6**, 1600451.
- 45 F. Bai, X. Yang, R. Li, B. Huang and W. Huang, *Polymer*, 2006, **47**, 5775–5784.
- 46 X. Zhao, R. Yu, H. Tang, D. Mao, J. Qi, B. Wang, Y. Zhang, H. Zhao, W. Hu and D. Wang, *Adv. Mater.*, 2017, **29**, 1700550.
- 47 P. Zhang, B. Y. Guan, L. Yu and X. W. Lou, *Angew. Chem., Int. Ed.*, 2017, **56**, 7141–7145.
- 48 Y. Huang, D. Wu, S. Han, S. Li, L. Xiao, F. Zhang and X. Feng, *ChemSusChem*, 2013, **6**, 1510–1515.
- 49 H. Kim, H. Kim, S. Muhammad, J. H. Um, M. S. A. Sher Shah, P. J. Yoo and W.-S. Yoon, *J. Power Sources*, 2020, **446**, 227321.